Multimode Organic Polariton Lasing

Kristin B. Arnardottir[1,*], Antti J. Moilanen[2], Artem Strashko[3], Päivi Törmä[2], and Jonathan Keeling[1]

[1]*SUPA, School of Physics and Astronomy, University of St Andrews, St Andrews KY16 9SS, United Kingdom*
[2]*Department of Applied Physics, Aalto University School of Science, P.O. Box 15100, Aalto FI-00076, Finland*
[3]*Center for Computational Quantum Physics, Flatiron Institute, 162 5th Avenue, New York, New York 10010, USA*

We present a beyond-mean-field approach to predict the nature of organic polariton lasing, accounting for all relevant photon modes in a planar microcavity. Starting from a microscopic picture, we show how lasing can switch between polaritonic states resonant with the maximal gain, and those at the bottom of the polariton dispersion. We show how the population of nonlasing modes can be found, and by using two-time correlations, we show how the photoluminescence spectrum (of both lasing and nonlasing modes) evolves with pumping and coupling strength, confirming recent experimental work on the origin of blueshift for polariton lasing.

By placing optically active organic material in a planar microcavity, one can create strong light-matter coupling, and thus new quasiparticles, exciton polaritons [1]. As seen in many materials [2,3], when pumped sufficiently, such polaritons transition to a "condensed" or lasing state, with macroscopic mode occupation and long range coherence. A wide variety of organic materials have shown polariton lasing [4–15] (for a review, see Ref. [16]). However, there are no general design rules for the optimal material properties for polariton lasing. Some key ideas have been identified through effective rate-equation modeling [17–21], showing how resonance with vibrational modes can play a key role in scattering from an excitonic reservoir to the polariton modes. However, such effective models leave open many questions, about weak-to-strong coupling crossover, the evolution of coherence and line shapes, or the competition between lasing modes.

Answering the above questions requires a microscopic model which captures competition between different cavity modes, and approaches beyond mean-field theory (MFT). These two requirements go hand in hand: fluctuation corrections to MFT grow with the number of photon modes. Single-mode models have been a popular and powerful tool [22–27]. However, because they only capture the macroscopically occupied modes, they cannot describe thermalization nor recover standard results for critical temperature in equilibrium. The relation between critical temperature and density for an equilibrium Bose-Einstein condensate arises because thermal populations of nonzero momentum states deplete the macroscopically occupied mode. Capturing such behavior requires considering fluctuation corrections to MFT, analogous to work on equilibrium excitonic condensates [28–31]. Here we extend this idea to incoherently pumped and decaying systems.

In this Letter, to realize the physics described above, we develop a second-order cumulant approach to describe the behavior of an organic polariton condensate. Using this we study the evolution of the system with pump strength and cavity detuning. We find a variety of different types of behavior, with lasing either near the bottom of the polariton dispersion or near resonance with the peak of the gain spectrum. By calculating two-time correlation functions, we present also a microscopic picture of how the polariton dispersion evolves with increasing pumping, giving direct predictions on the polariton blueshift.

Our model of organic molecules in multimode planar microcavities is illustrated in Fig. 1. Following Refs. [22,27] we model the N_{mol} molecules as vibrationally dressed emitters, placed randomly in a planar cavity, using an extended *multimode* Tavis-Cummings-Holstein Hamiltonian (i.e., in the rotating wave approximation):
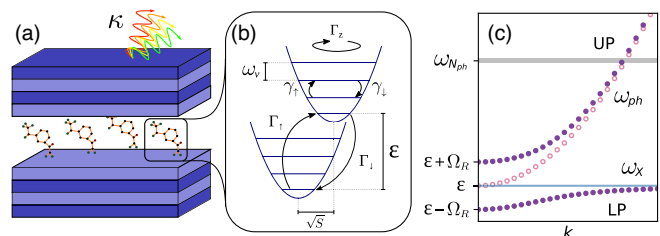

FIG. 1. (a) Organic molecules are placed inside a microcavity that supports multiple photon modes. (b) Molecular level structure and processes: Incoherent electronic pumping has rate $\Gamma_\uparrow$, electronic decay $\Gamma_\downarrow$, and dephasing Γ_z. The thermal (de)excitation rates of the vibrational modes are $\gamma_{\uparrow(\downarrow)}$. (c) Discretized photon dispersion. Integer k labels modes. Light-matter coupling hybridizes the photon (ω_k) and exciton (ε) into polariton modes. Figure plotted for $\omega_0 = \varepsilon$. We truncate the photon modes at $K = N_{modes}$ where the hybridization becomes weak.

$$H = \sum_n \left[\frac{\varepsilon}{2} \sigma_n^z + \omega_v(b_n^\dagger b_n + \sqrt{S}(b_n^\dagger + b_n)\sigma_n^z) \right]$$
$$+ \sum_{\mathbf{k}} \omega_{\mathbf{k}} a_{\mathbf{k}}^\dagger a_{\mathbf{k}} + \sum_{n,\mathbf{k}} (g_{n,\mathbf{k}} a_{\mathbf{k}} \sigma_n^+ + g_{n,\mathbf{k}}^* a_{\mathbf{k}}^\dagger \sigma_n^-). \quad (1)$$

The first line describes the organic molecules, labeled by site n. Here ε is the energy of the electronic transition, the Pauli matrices $\sigma_n^{z,\pm}$ describe the electronic state, while $b_n^\dagger$ creates a vibrational excitation (vibron) of energy ω_v. The vibronic coupling is characterized by the Huang-Rhys parameter S. For brevity we use below the notation $(n-m)$ to denote a transition between the electronic ground state with n vibrons, and the electronic excited state with m vibrons. The operator $a_{\mathbf{k}}^\dagger$ creates a photon with wave vector $\mathbf{k}$ and energy ω_k, and the light-matter coupling has strength $g_{n,\mathbf{k}}$; these are discussed in detail below. We ignore hopping of excitons between molecules as delocalization through coupling to light dominates over hopping [22,32].

To consider a finite number of photon modes we must consider a finite-sized simulation. We take the system to be a $L \times L$ square with periodic boundaries, so the photon modes are plane waves with $\mathbf{k} = (2\pi/L)(K_x, K_y)$, where K_x and K_y are integers. The coupling constants $g_{n,\mathbf{k}}$ then take the form $g_{n,\mathbf{k}} = ge^{-i\mathbf{k}\cdot\mathbf{r}_n}$, where $\mathbf{r}_n$ is the in-plane location of molecule n, discussed further below [33]. The coupling strength depends on the photon mode volume such that $g \sim 1/\sqrt{L^2}$, but as each photon mode couples to many molecules the overall light-matter coupling strength is better characterized by the Rabi splitting $\Omega_R = \sqrt{N_{\text{mol}}}g$, which will depend on the molecular density in the cavity plane $\rho_{2D} = N_{\text{mol}}/L^2$.

We may write the photon energies as $\omega_k = \omega_0 + E_\rho(K_x^2 + K_y^2)/N_{\text{mol}}$, where we have defined an energy scale $E_\rho = \pi^2 \rho_{2D} \hbar^2/2m$ in terms of the molecular density ρ_{2D} and effective photon mass m. The integers K_x, K_y will have an upper bound, as only those photon modes close enough to resonance with the molecules are relevant. Taking this condition to be $(\omega_{k_{\text{max}}} - \varepsilon) \gtrsim \Omega_R$ leads to a value $K_{\text{max}} \sim \sqrt{N_{\text{mol}}\Omega_R/E_\rho}$. Counting the total number of photon modes, N_{modes}, in a 2D system, $N_{\text{modes}} \propto K_{\text{max}}^2$ [34], so we find $N_{\text{modes}}/N_{\text{mol}} \sim \Omega_R/E_\rho$. This ratio is important, as it determines how well MFT works. For a single mode, fluctuation corrections to MFT are suppressed as $1/N_{\text{mol}}$. As we discuss below, adding more photon modes increases fluctuations, so that the relevant ratio is $N_{\text{modes}}/N_{\text{mol}}$. This same ratio also determines the relation between in-plane molecular separation Δr vs typical in-plane wavelength $\lambda_t \sim L/K_{\text{max}}$, i.e., $E_\rho/\Omega_R \sim (\lambda_t/\Delta r)^2$. For realistic systems E_ρ is typically of the order 10^5–10^6 eV [35], far greater than the typical value of $\Omega_R \simeq 1$ eV. For the numerical results in this Letter we have set $E_\rho = 5 \times 10^5$ eV [36].

Including the incoherent processes shown in Fig. 1, the equation of motion for the system density matrix is [27]

$$\partial_t \rho = -i[H,\rho] + \sum_{\mathbf{k}} \kappa \mathcal{L}[a_{\mathbf{k}}] + \sum_n (\Gamma_\uparrow \mathcal{L}[\sigma_n^+] + \Gamma_\downarrow \mathcal{L}[\sigma_n^-]$$
$$+ \Gamma_z \mathcal{L}[\sigma_n^z] + \gamma_\uparrow \mathcal{L}[b_n^\dagger - \sqrt{S}\sigma_n^z] + \gamma_\downarrow \mathcal{L}[b_n - \sqrt{S}\sigma_n^z]), \quad (2)$$

where $\mathcal{L}[X] = X\rho X^\dagger - \frac{1}{2}(X^\dagger X\rho + \rho X^\dagger X)$. We include photon loss at rate κ (assumed equal for all modes), and incoherent pumping, decay, and dephasing of molecules with rates $\Gamma_\uparrow$, $\Gamma_\downarrow$, and Γ_z respectively. The last two terms describe thermalization of vibrons, with rates $\gamma_\downarrow = \gamma_v(n_b + 1)$, $\gamma_\uparrow = \gamma_v n_b$, and $n_b = [\exp(\omega_v/k_b T_v) - 1]^{-1}$ is the Bose-Einstein distribution. Physically this corresponds to assuming that molecular vibrational modes rapidly thermalize by coupling to some effective external reservoir at temperature T_v, such as a solvent or the surrounding medium.

To capture both strong vibrational and light-matter coupling, we will combine two electronic and N vibrational levels into $2N$-level molecular operators for each molecule. A basis for such operators are the generalized Gell-Mann matrices [38], $\lambda_i^{(n)}$. Using these, the system Hamiltonian takes the form $H = \sum_{\mathbf{k}} \omega_k a_{\mathbf{k}}^\dagger a_{\mathbf{k}} + \sum_n [A_i + \sum_{\mathbf{k}}(B_i a_{\mathbf{k}}^\dagger e^{-i\mathbf{k}\cdot\mathbf{r}_n} + \text{H.c.})]\lambda_i^{(n)}$. Hereon, sums over repeated Gell-Mann matrix indices i are implicit. The form of the vectors A_i and B_i is determined by Eq. (1). Equation (2) can similarly be rewritten as $\partial_t \rho = -i[H,\rho] + \sum_{\mathbf{k}} \kappa \mathcal{L}[a_{\mathbf{k}}] + \sum_{\mu,n} \mathcal{L}[\gamma_i^\mu \lambda_i^{(n)}]$. Here μ runs over the different molecular dissipative processes (pump, decay, dephasing, and vibrational excitation and decay).

As noted above, mean-field (MF) approaches are useful to understand the linear stability of the normal state, but cannot yield information about the nonlasing modes, which ultimately can modify the critical properties of the lasing transition. In thermal equilibrium, this was studied by considering Gaussian fluctuation corrections to MFT [28–31]. There one finds that when fluctuation corrections are large, the critical temperature matches the degeneracy temperature of the 2D Bose gas, due to thermal depopulation of the condensate mode. The relative significance of fluctuations in those works depends on a dimensionless ratio, $m^* = m\Omega_R/\hbar^2\rho_{2D}$—meaning fluctuations are more significant when there is a large photon density of states. This quantity m^* is the same ratio as $N_{\text{modes}}/N_{\text{mol}}$, identified as controlling the role of beyond-mean-field effects. We will see that even in the general nonequilibrium context, this same parameter controls the effects of fluctuations. Given the small value we have for $N_{\text{modes}}/N_{\text{mol}}$, we may expect the effects of fluctuations will be small, but nonvanishing. A further discussion of the effects of changing this parameter is given in the Supplemental Material [37].

To go beyond MFT, we write second order cumulant equations; this means writing equations of motion for

second-order correlations of the operators $a_\mathbf{k}$, $a_\mathbf{k}^\dagger$, and $\lambda_i^{(n)}$, and splitting all higher order expectations into products of first and second order moments [39]. Such an approach directly relates to the semiclassical theory of lasing [40,41], and has been used to study the differences between lasing and condensation in the Dicke model [42,43], and to study Rabi oscillations [44]. As the Hamiltonian has $U(1)$ symmetry under a common phase change of $a_\mathbf{k}$ and σ_n^-, the cumulant equations will simplify if we split the λ_i into three groups: those that conserve, increase, or decrease the electronic excitations, denoted z, $+$, and $-$, respectively.

As yet, we have made no assumptions about the positions of molecules $\mathbf{r}_n$. At this point we use the earlier observation that there are many molecules within the typical in-plane wavelength; we may thus assume spatial homogeneity, and so approximate $\sum_n e^{i(\mathbf{k}-\mathbf{k}')\cdot\mathbf{r}_n} = N_{\mathrm{mol}}\delta_{\mathbf{k},\mathbf{k}'}$, giving conservation of momentum [45]. For single-mode lasing, this also leads to homogeneous populations, so that $\ell_i = \langle \lambda_{i_z}^{(n)} \rangle$ is independent of n. Similarly, we can write the Fourier components of the coherences $c_i^\mathbf{k} = \sum_n e^{i\mathbf{k}\cdot\mathbf{r}_n} \langle a_\mathbf{k} \lambda_{i_+}^{(n)} \rangle / N_{\mathrm{mol}}$ and $d_{ij}^\mathbf{k} = \sum_{n,m\neq n} e^{i\mathbf{k}\cdot(\mathbf{r}_n-\mathbf{r}_m)} \langle \lambda_{i_+}^{(n)} \lambda_{i_-}^{(m)} \rangle / N_{\mathrm{mol}}^2$. The equations of motion for these quantities, along with the photon occupations $n^\mathbf{k} = \langle a_\mathbf{k}^\dagger a_\mathbf{k} \rangle$ take the form

$$\partial_t n^\mathbf{k} = -\kappa n^\mathbf{k} - 2N_{\mathrm{mol}}\mathrm{Im}[B_i c_i^\mathbf{k}], \quad (3)$$

$$\partial_t \ell_i = \xi_{ij}\ell_j + \phi_i - 8\mathrm{Re}\left[\beta_{ij}\sum_k c_j^\mathbf{k}\right], \quad (4)$$

$$\partial_t c_i^\mathbf{k} = \left[X_{ij} - \left(i\omega_k + \frac{\kappa}{2}\right)\delta_{ij}\right]c_j^\mathbf{k} + 2\beta_{ij}^*\ell_j n_\mathbf{k}$$
$$- iB_j d_{ij}^\mathbf{k} - \frac{i}{N_{\mathrm{mol}}}\left(\zeta_{ij}\ell_j + \frac{B_i}{2N}\right), \quad (5)$$

$$\partial_t d_{ij}^\mathbf{k} = X_{ip}^* d_{pj}^\mathbf{k} + X_{jp} d_{ip}^\mathbf{k} + 2\ell_p(\beta_{ip}\tilde{c}_j^\mathbf{k} + \beta_{jp}^*\tilde{c}_i^\mathbf{k}), \quad (6)$$

where $\tilde{c}_i^\mathbf{k} = c_i^\mathbf{k} - \sum_\mathbf{q} c_i^\mathbf{q}/N_{\mathrm{mol}}$ and the coefficients $\xi_{ij}, X_{ij}, \phi_i, \beta_{ij}$, and ζ_{ij} are different combinations of the relevant structure constants, Hamiltonian constants, and decay rates, specified in the Supplemental Material [37]. By going beyond MF approaches, these equations now enable us to correctly capture the multimode behavior, and see how fluctuations modify the lasing threshold.

To get numerical results we have to fix values for the parameters of the system. We choose values, given in the caption of Fig. 2, which recover a realistic absorption and emission spectra in the weak-coupling regime—see Ref. [37]. To further reduce the problem size, we can project the $\mathbf{k}$ dependence of the equations onto one dimension. From hereon the integer K labels photon modes, with $|\mathbf{k}| = 2\pi K/L$, and a degeneracy factor W_K accounts for the two-dimensional density of states, see
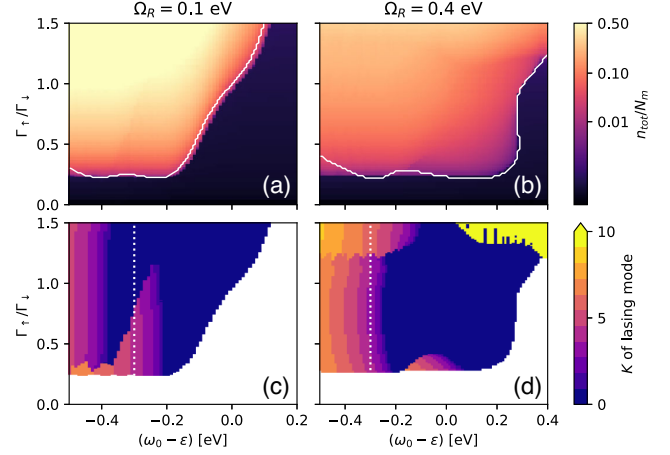

FIG. 2. Phase diagrams for the system at two values of the Rabi splitting Ω_R. The top row shows total photon occupation vs external pump rate (vertical) and the detuning of the photon dispersion from the zero vibron transition (horizontal). The white line is the single mode, MF linear stability result. The bottom row shows the K index of the highest occupied photon mode. The white dashed line indicates the parameters used in Figs. 3(a)–3(b). The parameters used here are $S = 0.1$, $\omega_v = 0.2$, $\Gamma_\downarrow = \kappa = 10^{-4}$, $\Gamma_z = 0.03$, $\gamma_v = 0.02$, and $k_b T_v = 0.025$ eV.

Ref. [37] for details. Figures 2(a)–2(b) show phase diagrams of total photon occupation, $n_{\mathrm{tot}} = \sum_K W_K n^K$, vs photon detuning ω_0 and pump $\Gamma_\uparrow$. Where MF predicts lasing (white line, from Ref. [27]) there is macroscopic occupation, while outside that region there is only occupation of order 1. The agreement between the MF and cumulant equations holds only because $N_{\mathrm{mol}} \gg N_{\mathrm{modes}}$; in Ref. [37] we show that for smaller N_{mol}, fluctuations push the transition to higher pump power. The only exception is in the bottom left corner, for values of ω_0 where MF predicts no lasing, but there exists a larger ω_0 which would show lasing at the same pump strength. In this case, the multimode model permits lasing of $K > 0$ modes. We find lasing at nonzero K occurs in other cases as well. Figures 2(c)–2(d) show which photon mode has the largest occupation n_K in the lasing region. In the case of weaker coupling ($\Omega_R = 0.1$ eV, left column), we find that when ω_0 is close to $(n - 0)$ transitions (i.e., for $\omega_0 = \varepsilon - n\omega_v$) for $n = 0$, 1, 2, lasing is predominantly in the $K = 0$ mode. For ω_0 between the (1-0) and (2-0) transitions there is competition between $K = 0$ and the mode, denoted K^* below, closest to resonance with the (1-0) transition.

To better see this competition, Fig. 3 shows n_K as a function of the pump for $\omega_0 = \varepsilon - 1.5\omega_v = 0.7$ eV. For weaker light-matter coupling, the growth of photon occupation is linear with pumping. The mode switching can then be explained by the competition of two potential lasing modes: the lowest mode $K = 0$ and a nonzero K mode, resonant with the (1-0) transition. Each mode has its own
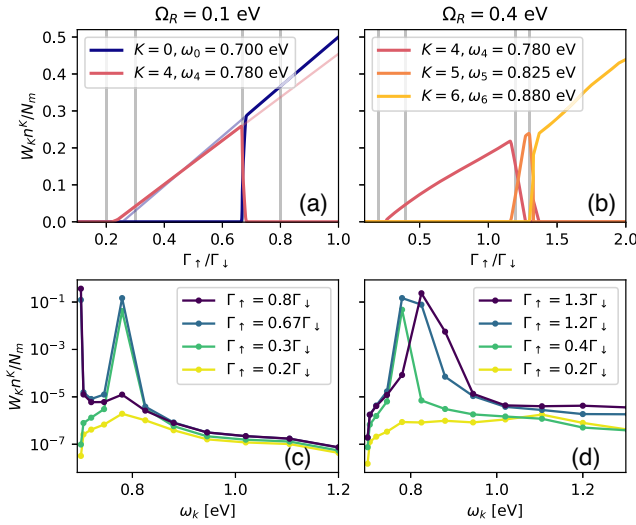
FIG. 3. Lasing mode switching for two different Rabi splittings Ω_R. The top row shows photon occupation as a function of external pump when ω_0 falls in between the (1-0) and (2-0) transitions $(\omega_0 - \varepsilon = -1.5\omega_v)$. (a) For Rabi splitting of $\Omega_R = 0.1$ eV, the nonzero vibron transitions (vibronic sidebands) are outside of the range of strong coupling. There is clear switching between two lasing modes, one close to (1-0) and the other at $K = 0$. Each mode that lases behaves linearly (a linear fit is shown by the thinner, fainter lines), similarly to textbook weak-coupling single-mode models. Reference [37] shows the threshold behavior on logarithmic scale. (b) For Rabi splitting of $\Omega_R = 0.4$ eV the lasing behavior is strongly influenced by the light-matter coupling, and the curves are no longer linear. The bottom row shows the occupation of all photon modes vs bare photon frequency ω_k, for the same values of ω_0 and Ω_R as in (a), (b), and pump strengths as marked by the gray vertical lines in panels (a),(b). Other parameters are the same as in Fig. 2.

threshold and slope efficiency (gradient of photon occupation vs pump). When two modes are above threshold, the mode with larger gain will suppress the other. There is a very narrow region of pump values where the gain is similar, which leads to coexistence [47]—macroscopic occupation of both modes—this can be seen from, e.g., $\Gamma_\uparrow = 0.67\Gamma_\downarrow$ line in Fig. 3(c). Another notable feature is that even at the lowest detunings, lasing never switches to a mode resonant with the (3-0) transition. This can be explained by the coupling to this transition being too weak, as the effective coupling to the $(n-0)$ transitions falls off as $\langle n|e^{\sqrt{S}(b^\dagger-b)}|0\rangle = S^{n/2}/\sqrt{n!}$.

At stronger light-matter coupling, as shown in the right columns of Figs. 2 and 3, the mode switching can no longer be described as a patchwork of single mode results. Figure 2(d) shows two interesting changes. First, there is a region of high K^* lasing for very high pump strength and positive detuning, and second, at large negative detuning there is switching between adjacent K^* modes. The high K^* lasing can be explained by the complete inversion of the two-level system, which implies net gain exists at both high

and low frequencies (away from the vibronic structure); photon modes at high K^* overlap with such gain. A large positive ω_0 is required to reach total inversion of the two-level systems, as otherwise, polariton lasing clamps $\langle\sigma^z\rangle < 0$. For further details see Ref. [37]. To understand the K^* switching we consider in detail the behavior seen in Fig. 3(b). Because for $\Omega_R = 0.4$ eV, the system remains in the strong coupling regime even when lasing (see below), we may note that even at a fixed K^*, the energies of the polaritons are known to shift to higher energy with increasing density (also discussed below). As such, the shift to higher K^* with increasing pump is at first surprising: lasing moves to higher energy modes, as each mode itself moves to higher energy. The explanation of this requires the observation that with increasing pumping, the gain spectrum also shifts to higher energies. This happens because the sequence of $(n - 0)$ vibrational sidebands, with decreasing n and thus increasing energy, become inverted in turn as pumping increases.

As already noted, due to strong light-matter coupling, the mode energies are those of polaritons, not bare photons and excitons. Moreover, because of the saturability of two-level systems, these polariton energies are density dependent, showing a blueshift of the lower polariton with increasing pumping. To find the energy of the occupied modes, we can calculate the photoluminescence (PL) spectrum:

$$S_\mathbf{k}(\nu) = \int_{-\infty}^{\infty} dt \langle a_\mathbf{k}^\dagger(t)a_\mathbf{k}(0)\rangle e^{i\nu t}. \qquad (7)$$

This can be found by the quantum regression theorem [41]: Using the steady state density matrix ρ_{ss}, we construct $\tilde\rho(0) = a_\mathbf{k}\rho_{ss}$, time evolve $\tilde\rho$, and then evaluate
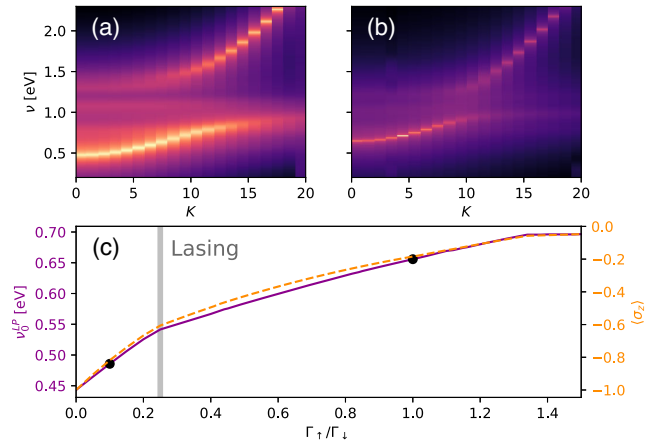

FIG. 4. (a)–(b) Photoluminescence spectra of the system for (a) $\Gamma_\uparrow = 0.1\Gamma_\downarrow$ and (b) $\Gamma_\uparrow = \Gamma_\downarrow$. (c) The energy of the lower polariton branch ν_0^{LP} (purple, solid line, left axis) and $\langle\sigma^z\rangle$ (dashed, orange line, right axis) vs pump strength. The black dots correspond to the pump values in panels (a)–(b) above, and the gray line marks the lasing threshold.

$\text{Tr}[a_\mathbf{k}^\dagger \tilde{\rho}(t)]$. Within our cumulant approximation, this gives a set of coupled differential equations for two-time correlators, with a form similar to Eqs. (3)–(6), see Ref. [37].

Example PL spectra are shown in Figs. 4(a) and 4(b), for parameters matching the strong light-matter coupling shown in Fig. 3(b). Panel (a) corresponds to a small pumping while (b) shows larger pumping in the lasing regime. The peaks in the spectra correspond to the system's mode energies, their widths to the lifetimes, and intensities to the occupations. The polariton anticrossing is clearly visible in both spectra, indicating strong coupling persists, but the splitting is reduced at higher pumping, corresponding to a blueshift of the lower polariton branch. In contrast, for $\Omega_R = 0.1$ eV, the polariton splitting collapses before lasing occurs. We may note that even when strong coupling is seen, a broad feature at the bare exciton energy is visible. This corresponds to uncoupled excitonic "dark states," which are known to become optically active due to the vibronic coupling [24,48,49]. We can study the blueshift by extracting the lower polariton frequency at $K = 0$ for different pumping strengths, as seen in Fig. 4(c) in solid (purple)—see Ref. [37] for details. By comparing the lower polariton energy to the inversion $\langle \sigma_z \rangle$ (dashed, orange line) it is clear that the blueshift seen here corresponds entirely to the saturation of the molecular optical transition.

In this Letter we have shown how the nature of organic polariton lasing changes with changing pump, detuning, and light-matter coupling. To understand this fully requires consideration of the multiple photon modes in a planar microcavity, which in turn demands a treatment beyond MFT, which we have introduced here. We find switching between different lasing modes, which can be understood via the slope efficiencies of different modes, and the evolution of gain profile. Our approach allows direct calculation of the PL spectrum of the driven system, giving information on the lasing frequency and the evolution of the polariton dispersion, distinguishing photon and polariton lasing. Using our microscopic model, we could show that the blueshift closely matches the occupation of the exciton ground state, corroborating the phenomenological saturation model of polariton interaction [15]. The methods described in this Letter can straightforwardly be extended to more complex molecules (e.g., other electronic states, further vibrational modes, or other dissipative processes), or to analysis of time-dependent pumping which we will discuss in a subsequent publication. As such, this provides a foundation to predict how molecular properties determine the optimal materials for organic polariton lasing.

The research data underpinning this publication can be accessed at [50].

[*] kba3@st-andrews.ac.uk

[1] V. M. Agranovich, *Excitations in Organic Solids* (Oxford University Press, Oxford, 2009).

[2] I. Carusotto and C. Ciuti, Quantum fluids of light, Rev. Mod. Phys. **85**, 299 (2013).

[3] D. Sanvitto and S. Kéna-Cohen, The road towards polaritonic devices, Nat. Mater. **15**, 1061 (2016).

[4] S. Kéna-Cohen and S. Forrest, Room-temperature polariton lasing in an organic single-crystal microcavity, Nat. Photonics **4**, 371 (2010).

[5] J. D. Plumhof, T. Stöferle, L. Mai, U. Scherf, and R. F. Mahrt, Room-temperature Bose-Einstein condensation of cavity exciton-polaritons in a polymer, Nat. Mater. **13**, 247 (2014).

[6] K. S. Daskalakis, S. A. Maier, R. Murray, and S. Kéna-Cohen, Nonlinear interactions in an organic polariton condensate, Nat. Mater. **13**, 271 (2014).

[7] C. P. Dietrich, A. Steude, L. Tropf, M. Schubert, N. M. Kronenberg, K. Ostermann, S. Höfling, and M. C. Gather, An exciton-polariton laser based on biologically produced fluorescent protein, Sci. Adv. **2**, e1600666 (2016).

[8] T. Cookson, K. Georgiou, A. Zasedatelev, R. T. Grant, T. Virgili, M. Cavazzini, F. Galeotti, C. Clark, N. G. Berloff, D. G. Lidzey, and P. G. Lagoudakis, A yellow polariton condensate in a dye filled microcavity, Adv. Opt. Mater. **5**, 1700203 (2017).

[9] G. Lerario, A. Fieramosca, F. Barachati, D. Ballarini, K. S. Daskalakis, L. Dominici, M. De Giorgi, S. A. Maier, G. Gigli, S. Kéna-Cohen, and D. Sanvitto, Room-temperature superfluidity in a polariton condensate, Nat. Phys. **13**, 837 (2017).

[10] M. Ramezani, A. Halpin, A. I. Fernández-Domínguez, J. Feist, S. R.-K. Rodriguez, F. J. Garcia-Vidal, and J. G. Rivas, Plasmon-exciton-polariton lasing, Optica **4**, 31 (2017).

[11] F. Scafirimuto, D. Urbonas, U. Scherf, R. F. Mahrt, and T. Stöferle, Room-temperature exciton-polariton condensation in a tunable zero-dimensional microcavity, ACS Photonics **5**, 85 (2018).

[12] S. K. Rajendran, M. Wei, H. Ohadi, A. Ruseckas, G. A. Turnbull, and I. D. W. Samuel, Low threshold polariton lasing from a solution-processed organic semiconductor

in a planar microcavity, Adv. Opt. Mater. **7,** 1801791 (2019).

[13] M. Wei, S. K. Rajendran, H. Ohadi, L. Tropf, M. C. Gather, G. A. Turnbull, and I. D. W. Samuel, Low threshold polariton lasing in a highly disordered conjugated polymer, Optica **6,** 1124 (2019).

[14] A. I. Väkeväinen, A. J. Moilanen, M. Nečada, T. K. Hakala, K. S. Daskalakis, and P. Törmä, Sub-picosecond thermalization dynamics in condensation of strongly coupled lattice plasmons, Nat. Commun. **11,** 3139 (2020).

[15] T. Yagafarov, D. Sannikov, A. Zasedatelev, K. Georgiou, A. Baranikov, O. Kyriienko, I. Shelykh, L. Gai, Z. Shen, D. G. Lidzey, and P. Lagoudakis, Mechanisms of blueshifts in organic polariton condensates, Commun. Phys. **3,** 18 (2020).

[16] J. Keeling and S. Kéna-Cohen, Bose–Einstein condensation of exciton-polaritons in organic microcavities, Annu. Rev. Phys. Chem. **71,** 435 (2020).

[17] P. Michetti and G. C. La Rocca, Exciton-phonon scattering and photoexcitation dynamics in J-aggregate microcavities, Phys. Rev. B **79,** 035325 (2009).

[18] L. Fontanesi, L. Mazza, and G. C. La Rocca, Organic-based microcavities with vibronic progressions: Linear spectroscopy, Phys. Rev. B **80,** 235313 (2009).

[19] L. Mazza, L. Fontanesi, and G. C. La Rocca, Organic-based microcavities with vibronic progressions: Photoluminescence, Phys. Rev. B **80,** 235314 (2009).

[20] L. Mazza, S. Kéna-Cohen, P. Michetti, and G. C. La Rocca, Microscopic theory of polariton lasing via vibronically assisted scattering, Phys. Rev. B **88,** 075321 (2013).

[21] D. M. Coles, P. Michetti, C. Clark, W. C. Tsoi, A. M. Adawi, J.-S. Kim, and D. G. Lidzey, Vibrationally assisted polariton-relaxation processes in strongly coupled organic-semiconductor microcavities, Adv. Funct. Mater. **21,** 3691 (2011).

[22] J. A. Ćwik, S. Reja, P. B. Littlewood, and J. Keeling, Polariton condensation with saturable molecules dressed by vibrational modes, Europhys. Lett. **105,** 47009 (2014).

[23] J. Galego, F. J. Garcia-Vidal, and J. Feist, Cavity-Induced Modifications of Molecular Structure in the Strong-Coupling Regime, Phys. Rev. X **5,** 041022 (2015).

[24] F. Herrera and F. C. Spano, Dark Vibronic Polaritons and the Spectroscopy of Organic Microcavities, Phys. Rev. Lett. **118,** 223601 (2017).

[25] J. del Pino, F. A. Y. N. Schröder, A. W. Chin, J. Feist, and F. J. Garcia-Vidal, Tensor Network Simulation of Non-Markovian Dynamics in Organic Polaritons, Phys. Rev. Lett. **121,** 227401 (2018).

[26] J. del Pino, F. A. Y. N. Schröder, A. W. Chin, J. Feist, and F. J. Garcia-Vidal, Tensor network simulation of polaron-polaritons in organic microcavities, Phys. Rev. B **98,** 165416 (2018).

[27] A. Strashko, P. Kirton, and J. Keeling, Organic Polariton Lasing and the Weak to Strong Coupling Crossover, Phys. Rev. Lett. **121,** 193601 (2018).

[28] P. Nozières and S. Schmitt-Rink, Bose condensation in an attractive fermion gas: From weak to strong coupling superconductivity, J. Low Temp. Phys. **59,** 195 (1985).

[29] M. Randeria, Crossover from BCS theory to Bose–Einstein condensation, in *Bose–Einstein Condensation*, edited by A. Griffin, D. Snoke, and S. Stringari (Cambridge University Press, Cambridge, England, 1995), p. 355.

[30] J. Keeling, P. R. Eastham, M. H. Szymańska, and P. B. Littlewood, Polariton Condensation with Localized Excitons and Propagating Photons, Phys. Rev. Lett. **93,** 226403 (2004).

[31] J. Keeling, P. R. Eastham, M. H. Szymanska, and P. B. Littlewood, BCS-BEC crossover in a system of microcavity polaritons, Phys. Rev. B **72,** 115320 (2005).

[32] M. Nečada, J.-P. Martikainen, and P. Törmä, Quantum emitter dipole–dipole interactions in nanoplasmonic systems, Int. J. Mod. Phys. B **31,** 1740006 (2017).

[33] We assume molecules are confined near the middle of the cavity and so ignore the mode profile across the cavity.

[34] J. del Pino, J. Feist, and F. J. Garcia-Vidal, Quantum theory of collective strong coupling of molecular vibrations with a microcavity mode, New J. Phys. **17,** 053040 (2015).

[35] E. Eizner, L. A. Martínez-Martínez, J. Yuen-Zhou, and S. Kéna-Cohen, Inverting singlet and triplet excited states using strong light-matter coupling, Sci. Adv. **5,** eaax4482 (2019).

[36] Combined with $N_{mol} = 10^8$ and $\hbar^2/2m = 5 \times 10^{-4}$ eV μm^2 (consistent with $\omega_0 \sim 1$ eV), this corresponds for example to $L \sim 1$ μm. This is large enough that finite-ize effects are small; for results with larger L, see Ref. [37].

[37] See Supplemental Material at http://link.aps.org/supplemental/10.1103/PhysRevLett.125.233603 for derivation of the cumulant equations, results showing how molecule number affects accuracy of mean field theory, details of the high-k lasing at large pump power, and details of calculation of the photoluminescence spectrum.

[38] M. Stone and P. Goldbart, *Mathematics for Physics: A Guided Tour for Graduate Students* (Cambridge University Press, Cambridge, England, 2009).

[39] C. Gardiner, *Stochastic Methods: A Handbook for the Natural and Social Sciences*, Springer Series in Synergetics (Springer, Berlin, Heidelberg, 2009).

[40] H. Haken, The semiclassical and quantum theory of the laser, in *Quantum Optics*, edited by S. M. Kay and A. Maitland (Academic Press, New York, 1970), p. 201.

[41] M. O. Scully and M. S. Zubairy, *Quantum Optics* (Cambridge University Press, Cambridge, England, 1997).

[42] P. Kirton and J. Keeling, Suppressing and Restoring the Dicke Superradiance Transition by Dephasing and Decay, Phys. Rev. Lett. **118,** 123602 (2017).

[43] P. Kirton and J. Keeling, Superradiant and lasing states in driven-dissipative Dicke models, New J. Phys. **20,** 015009 (2018).

[44] M. Sánchez-Barquilla, R. E. F. Silva, and J. Feist, Cumulant expansion for the treatment of light–matter interactions in arbitrary material structures, J. Chem. Phys. **152,** 034108 (2020).

[45] Disorder can localize states at points where the polariton dispersion becomes flat [46]. This would affect the spatial (and momentum) profile of condensed modes, but not the basic picture of mode competition and thermalization we consider here, so we neglect this.

[46] M. Litinskaya and P. Reineker, Loss of coherence of exciton polaritons in inhomogeneous organic microcavities, Phys. Rev. B **74**, 165320 (2006).

[47] The assumption of single-mode operation used in Eqs. (3)–(6) will break down in this coexistence region; however, this region is very narrow, so we do not expect significant deviations to arise.

[48] J. A. Ćwik, P. Kirton, S. De Liberato, and J. Keeling, Excitonic spectral features in strongly coupled organic polaritons, Phys. Rev. A **93**, 033840 (2016).

[49] M. A. Zeb, P. G. Kirton, and J. Keeling, Exact states and spectra of vibrationally dressed polaritons, ACS Photonics **5**, 249 (2017).

[50] K. B. Arnardottir, A. Molianen, A. Strashko, P. Törmä, and J. M. J. Keeling, Data underpinning: Multimode organic polariton lasing, Dataset, University of St Andrews Research Portal, https://doi.org/10.17630/541eb0b3-dd8a-4e03-a212-b349ae233770.